Novel photofragment spectrometer for the investigation of molecular three-body decay

M. Braun, M. Beckert, and U. Müller[a)]
Universität Freiburg, Fakultät für Physik, Stefan-Meier-Strasse 19, D-79104 Freiburg, Germany

(Received 12 May 2000; accepted for publication 2 August 2000)

We have developed a novel photofragment spectrometer to investigate the fragmentation of neutral molecules into two, three, and more neutral fragments. The parent molecules are laser prepared in a fast beam. The photofragments are detected in coincidence by a time- and position-sensitive detector which consists of multichannel plates and delay line anodes. We have developed new electronic pulse routers which allow us to measure consecutive fragment hits with dead times as low as a few nanoseconds. A new algorithm has been developed to determine for each triple hit the momentum vectors of the three fragments from the measured arrival time differences and positions. To demonstrate the performance of the spectrometer, we have investigated two- and three-body decay processes of laser-prepared triatomic hydrogen molecules H_3 into $H+H_2$ fragment pairs as well as into three hydrogen atoms $H(1s)+H(1s)+H(1s)$. For two-body decay of vibrationless H_3 $3s^2A_1'(N=1,\ K=0)$, we have found that the resolution in the kinetic energy release spectra is far better than that achieved in previous investigations. With the new spectrometer, kinematically complete investigations of the breakup of a neutral molecule into three neutral fragments have been performed. The final state distributions in the three body decay of laser-prepared H_3 molecules show pronounced structures which give insight into the complex molecular decay mechanisms. © *2000 American Institute of Physics.* [S0034-6748(00)02111-0]

I. INTRODUCTION

The dissociation of a molecule into neutral products plays an important role in astrophysics and plasma physics. The formation of neutral fragments slowly receding from the center-of-mass allows to study the correlation of the fragment momentum vectors which reflects the decay dynamics on the repulsive potential energy surfaces. In contrast to breakup processes into charged particles, the momentum correlations between neutral fragments are not affected by long-range post-collisional interaction. In the case of larger molecules, dissociation into three and more massive fragments may constitute a major decay pathway.[1–5] To understand the dynamics of such processes, the parent molecule has to be prepared in a quantum mechanically well-characterized initial state. To achieve a kinematically complete analysis of the final state, all fragments have to be detected in coincidence. Such investigations constitute a substantial challenge to experimental technique. Multihit coincidence experiments of atomic and molecular processes have only recently become feasible by the progress of time- and position-sensitive particle detectors which combine large detection areas with high spatial and temporal resolution. Momentum correlations in the final states of atomic double- and multiple-ionization have recently been studied[6,7] using such detectors. Time- and position-sensitive detectors also play an important role in molecular Coulomb explosion studies.[8–12]

To investigate laser-induced molecular dissociation, velocity map imaging techniques have been developed. However, these experiments are not applicable to coincidence studies, and they need a laser-postionization step to detect neutral photodissociation products.[13–16] Fast-beam techniques are elegant methods to study the formation of neutral fragments. Because of their translational energy, the dissociation products can be detected by microchannel plates and time- and position-sensitive anodes. Translational spectroscopy using time- and position-sensitive detectors was pioneered by de Bruijn and Los[17] and applied to study dissociative charge transfer of H_2^+ and N_2^+.[18] The production of fast neutral molecular beams by photodetachment of negative ions[19] has been pursued by groups in Berkeley[20] and San Diego.[21,22]

Laser excitation of fast metastable molecules allows to prepare the initial state in a well-defined quantum state. This has been widely applied to study molecular two-body breakup.[23–26] To investigate dissociation into three and more particles, a multihit coincidence detector is required which measures the arrival times and positions of all fragments with high accuracy and dead times as low as a few nanoseconds. Different types of time- and position sensitive detectors have been developed. Position sensitive anodes based on charge division (resistive anodes, wedge-and-strip anodes) achieve good spatial resolution but have comparatively long recovery times (several microseconds). Such anodes are not suitable for multihit applications, unless the sensitive area is subdivided and covered by several independent detector systems which greatly increases the hardware expenses. Using multielement anodes with individual readout circuits for each element, excellent multihit capabilities have been demonstrated[27] but the spatial resolution was only about 1

a)Electronic mail: Ulrich.Mueller@uni-freiburg.de

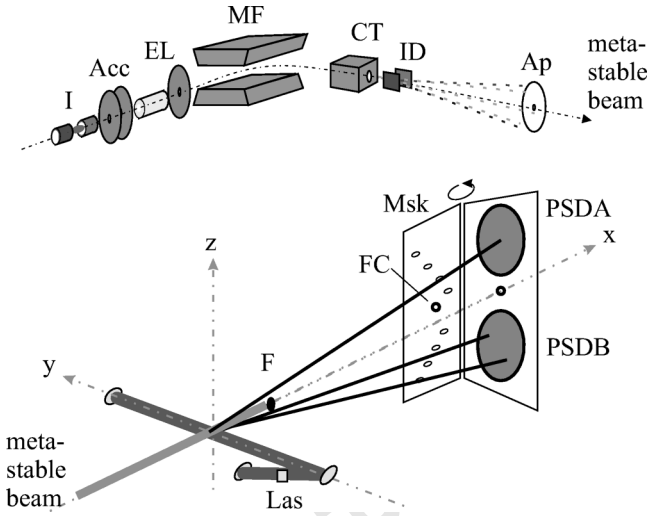

FIG. 1. Fast-beam laser-photofragment spectrometer for the investigation of molecular many-body dissociation processes. Legend: I: source, Acc: ion beam extraction and acceleration stage, EL: Einzel lens, MF: magnetic sector, CT: charge transfer cell, ID: ion deflector, Ap: aperture, Las: intracavity dye laser, F: beam stop, PSDA, PSDB: multihit time and position sensitive detectors with delay line anodes, Msk: mask for position calibration, FC: Faraday cup.

mm. An imaging detector which combines a phosphor screen and a CCD camera with multianode photomultipliers has been developed by Amitay and Zajfman.[28] This detector offers multihit capabilities and good time and position resolution, but the total event rate is limited by the camera readout (50 frames/s).

In our new fast-beam photofragment spectrometer, we use a position sensitive delay line anode.[29,30] In this detector type, the position of the fragment hits is determined by measuring arrival time differences of electromagnetic pulses. The detector achieves good position resolution, and the dead times after the events may be as low as a few nanoseconds at reasonable hardware costs. In the following, we first present our apparatus and the electronic readout circuit. Then, we describe the position and time calibration of the detector and the multihit data reduction to determine the fragment momentum vectors in translational spectroscopy. We discuss suitable projections of the multidimensional photodissociation cross sections to gain insight into the decay dynamics. To demonstrate the performance of the apparatus and the data evaluation procedure, we have investigated the laser photodissociation of the triatomic hydrogen molecule H_3. We present a kinematically complete final state analysis of the two-body decay into $H+H_2$ as well as the three-body decay into three hydrogen atoms $H(1s)+H(1s)+H(1s)$.

II. EXPERIMENT

A. Neutral and laser beam

A schematic diagram of the photofragment spectrometer recently developed in Freiburg is shown in Fig. 1. Molecular ions are created in a hollow cathode discharge source (I). The length of the cathode is 1.5 cm and the diameter is 1.2 cm. The source is operated at a pressure of about 1 mbar (10^{-2} Pa) and the cathode is water cooled to about 15 °C. The ions are extracted through a Pierce electrode with an aperture of about 150 μm diameter biased positively by 20–30 V relative to the anode. By operating the ion source with H_2, we produce rotationally and vibrationally cold H_3^+ ions. The ions are accelerated (Acc) to an energy selected between 3.0 and 6.0 keV and focused by an Einzel lens (EL). A mass selection is performed by a 90° magnetic sector (MF). A small fraction of the molecular ions is neutralized by charge transfer in cesium vapor. After the charge-transfer cell (CT), the unreacted ions are removed by an electric field (ID). In a distance of 30 cm downstream of the charge transfer cell, the products of dissociative charge transfer are stopped, and a well-collimated beam of metastable molecules is formed by an aperture (Ap) of 300 μm diameter.

The metastable beam is excited by a home-built standing wave dye laser (Las) pumped by an argon-ion laser. To take advantage of the high intracavity power, the neutral beam is crossed with the laser cavity. The vacuum chamber is equipped with Brewster windows to minimize the cavity losses. The spatial overlap between the laser beam and the neutral beam is optimized by raising or lowering the laser table. The laser wavelength is determined by a birefringent filter which is tuned by a stepping motor under computer control. For operation at a fixed wavelength, an intracavity etalon is inserted to reduce the laser bandwidth to about 0.1 cm^{-1}. The laser beam can be turned on and off by a beam shutter operated under computer control. This allows us to collect the events from metastable decay separately for later correction of the experimental data.

The photofragments which separate from each other due to their kinetic energy in the center-of-mass frame are detected in coincidence by a time- and position-sensitive multihit detector (PSDA, PSDB) after a free flight of about 150 cm. The undissociated part of the neutral beam is intercepted by a beam flag (F) in a distance of 10 cm from the laser-interaction region. The charge transfer cell (CT), the aperture (Ap), and the beam flag (F) are mounted on translational stages and are precisely aligned on the central (x) axis of the apparatus.

B. Photofragment detector

The time- and position-sensitive multihit detector for fast neutral fragments shown in Fig. 1 consists of two identical units (PSDA) and (PSDB). Two circular sensitive regions with a diameter of 44 mm, respectively, are centered on the y axis in distances of 35 mm from the x axis. They consist of Z stacks of multichannel plates (MCP) with 50 mm outside diameter and 25 μm channel diameter (Galileo). The units are supported by a rigid frame which can be rotated about the y and z axis by translational vacuum feedthroughs. A diode laser beam enters the vacuum chamber through a window, passes a 1 mm diameter aperture in the detector center and is aligned parallel to the neutral beam (x) direction. A small glass plate is mounted on the frame which supports the multichannel plates to reflect a part of the diode laser beam. This allows us to align the sensitive area of the detector perpendicular to the neutral beam (x) direction with an accuracy better than 2 mrad.

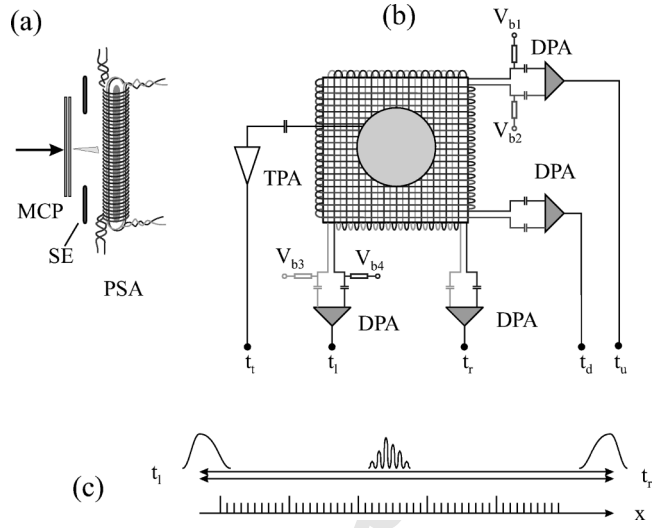

FIG. 2. Multihit time- and position-sensitive detector unit. Schematic side view (a), front view (b). Spacers, insulators, and supporting structures are omitted for clarity of presentation. The principle of the position measurement is shown in (c). Legend: MCP: multichannel plates, SE: shaping electrode, PSA: position sensitive delay line anode, TPA: fast preamplifier for timing signal, DPA: differential preamplifiers for position signals.

For calibration of the position scale (Sec. II D), a stainless steel mask (Msk) with a precisely machined hole pattern is placed in front of the detector. The mask is mounted on a hinge and can be placed and removed by a rotary feedthrough without breaking the vacuum. A Faraday cup (FC) mounted in the center of the mask allows us to detect and align the neutral beam. One of the time- and position-sensitive detector units is schematically shown in Fig. 2. Spacers, supporting elements, and insulators are omitted for clarity of presentation. The electron charge cloud from the MCPs is collected by a position sensitive delay line anode (PSA) in a distance of 15 mm. The shaping element (SE) is biased appropriately (+120 V) to minimize distortions of the extraction field at the border of the MCP. Position sensitive delay line anodes have been introduced by Sobodka and Williams.[29] The delay line anodes in our apparatus have been developed by Jagutzki *et al.*[30] As shown in Fig. 2, two waveguides are formed by pairs of parallel copper wires with 100 μm diameter and 1 mm distance. They are wrapped in two layers around a base plate of 80–80 mm^2 area made from copper. The total length of the wires is 8 m. They are held in place separated from each other and from the base plate by ceramics spacers. The distances of the layers for the two coordinates are 3 and 4 mm from the base plate, respectively. The wires of the first layer are biased by $V_{b1}=+215$ and $V_{b2}=+240$ V, respectively, those of the second layer by $V_{b2}=+225$ and $V_{b2}=+250$ V, respectively, relative to the exit of the multichannel plates. The base plate is held on a voltage of -500 V to repel the electrons. The different bias voltages lead to an imbalance of the amount of charge collected by the wires which form a waveguide. Electromagnetic pulses are excited and propagate to the ends of the waveguides. The waveguide terminals are connected by impedance matched twisted-pair lines and vacuum feedthroughs to capacitively coupled differential amplifiers (DPA), respectively. The delay line anode transforms the position of the electron cloud into arrival times (t_l,t_r,t_u,t_d) of electromagnetic pulses. The principle of the position measurement is shown in Fig. 2(c) for one dimension. For a waveguide of length L and effective group velocity v_g, the relations between the arrival times t_l,t_r of the pulses at the left and right end produced by a hit at position x and time t_0 are

$$t_l=t_0+(L/2+x)/v_g, \quad t_r=t_0+(L/2-x)/v_g. \tag{1}$$

The electron cloud from the MCPs covers several adjacent windings of the same waveguide. Due to a slight group velocity dispersion, the contributions from the individual windings melt together to a smooth output pulse. Using Eq. (1), we can determine the hit position x from the times t_l and t_r of the output pulses by

$$x=(t_l-t_r)v_g/2, \tag{2}$$

with a resolution much better than the separation of the waveguide windings. From Eq. (1), we can also determine the time t_0 of the event

$$t_0=(t_l+t_r-L/v_g)/2. \tag{3}$$

However, the time measurement by Eq. (3) is affected by the transit time spread of the electron cloud traveling from the MCPs to the anode, and the accuracy is not sufficient for our application. Therefore, timing pulses (t_t) are capacitively decoupled from the MCPs and guided by coaxial cables and impedance-matched vacuum feedthroughs to fast preamplifiers (TPA in Fig. 2). The time t_0 in Eq. 3 which can be determined for both Cartesian coordinates is used for a consistency check.

C. Readout system

The computer-controlled readout system for the time- and position-sensitive detectors is schematically shown in Fig. 3. The output pulses of the differential- and the timing amplifiers (PA) are converted to NIM-standard pulses by constant-fraction (CF) discriminators (Phillips Mod 715). The CF discriminators can be inhibited by the trigger logic (TL) via veto inputs (Veto). To measure the pulse arrival times, we use 12-bit time-to-digital converters (TDC) with eight channels, respectively (CAEN, V488a). The TDCs are triggered by a common start input (NIM pulses) and measure on each of the eight stop inputs the arrival times of the first pulses (ECL), respectively. The time resolution can be selected between 25 and 125 ps. During the time of conversion, the TDCs generate busy signals (Busy, active-high TTL) which are used in the trigger logic (TL). TDC_1 and TDC_2 measure the position information of detectors PSDA and PSDB, respectively, and are triggered by the corresponding timing signals. TDC_3 measures the time differences between the events and is triggered by the first timing pulse of PSDA. The timing pulses of the detector PSDB are amplified by a logic fanout (FO) and are routed to two stop inputs of TDC_3 via 450 and 50 ns long cable delays (Del_1, Del_2). This extends the range of the time measurement and allows to measure negative time differences which occur if the first fragment hits PSDB.

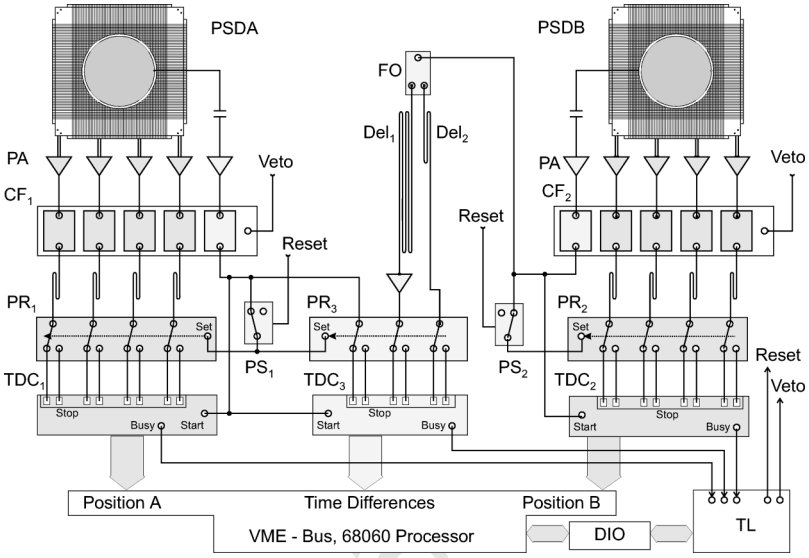

FIG. 3. Readout circuit of multihit time- and position-sensitive detector. Legend: PSDA, PSDB: time- and position sensitive delay line detector units, PA: preamplifiers, CF: constant-fraction discriminators, FO: pulse amplifier (fan-out), Del: cable delays, PR: pulse routers, PS: pulse selectors, TDC: time-to-digital converters, TL: trigger logic, DIO: digital input/output interface.

For the detection of multiple hits on both detector units, pulse routers (PR in Fig. 3) are provided for all position and timing signals. Since an individual TDC channel is stopped by the first pulse after the common start, the pulse routers (PR) distribute consecutive pulses to different TDC stop inputs. The pulse routers are designed in ECL technology. They allow time measurements with an accuracy corresponding to the resolution of the TDCs and a dead time between two pulses as low as 10 ns. The pulse routers also perform the conversion from NIM to ECL level required by the TDCs. The circuits and logic functions of the pulse routers (PR) and the pulse selectors (PS) are explained in Sec. II C 1. The system is currently equipped for the detection of double hits on each detector unit and can be easily extended by adding more TDCs.

The control of the experiment, the data readout, and the data preanalysis are performed by a dedicated processor (MC 68060 on Eltec Mod. BAB60 processor board). The data readout is synchronized by the trigger logic (TL in Fig. 3) which is connected to a digital interface (DIO). The circuit diagram and the timing sequence of the trigger logic are discussed in Sec. II C 2. The pulse routers, the TDCs, the processor board, and the digital interface are mounted in a VME crate.

1. Pulse routers

The circuit diagram of the pulse routers designed in ECL technology is shown in Fig. 4(a). The NIM-level input pulses are converted to active-low ECL pulses by transistors (not shown). These pulses (IN) are distributed to the clock inputs (CP_1, CP_2) of two *JK*-flipflops (FF_1,FF_2)and to the A_1, A_2, and A_3 inputs of three OR gates (OR_1, OR_2, OR_3). The $\overline{J}$ and $\overline{K}$ inputs of FF_1 are hard-wired to logic 1 and logic 0, respectively. The $\overline{J}$ and $\overline{K}$ inputs of FF_2 are connected to the $\overline{Q}$ and Q outputs of FF_1. The B_1 input of OR_1 is hard wired to logic 0. The B_2 and B_3 inputs of the OR gates OR_2 and OR_3 are connected to the outputs Q_1 and Q_2 of the flipflops FF_1 and FF_2, respectively.

The functional behavior is shown in the timing diagram Fig. 4(b). The flipflops FF_1 and FF_2 form a shift register which is programmed at the input to logic 0 status. A common set input (SET) switches the Q outputs of both flipflops to logic 1. The outputs Q_1 and Q_2 of the flipflops toggle to logic 0 on the trailing edges of the first and the second input pulses (IN), respectively. The output Y_2 of gate OR_2 remains logic 1 as long as Q_1 is logic 1. As soon as flipflop FF_1 toggles, Y_2 assumes the logic status of the input (IN). As a consequence, the second and all consecutive input pulses appear at the output of gate OR_2. In a similar way, the third and all consecutive input pulses appear at the output of gate OR_3. The output of gate OR_1 always assumes the logic status of the input (IN). The purpose of OR_1 is to equalize the propagation delays for all output signals. By connecting the outputs O_1, O_2, and O_3 of the pulse router to different TDC stop inputs, we can determine the arrival times of three consecutive input pulses (IN). The pulse router can be extended to an arbitrary number of consecutive pulses by adding more flipflops and OR gates.

In principle, the common set pulse (SET) to the pulse routers can be generated by the computer at the end of each

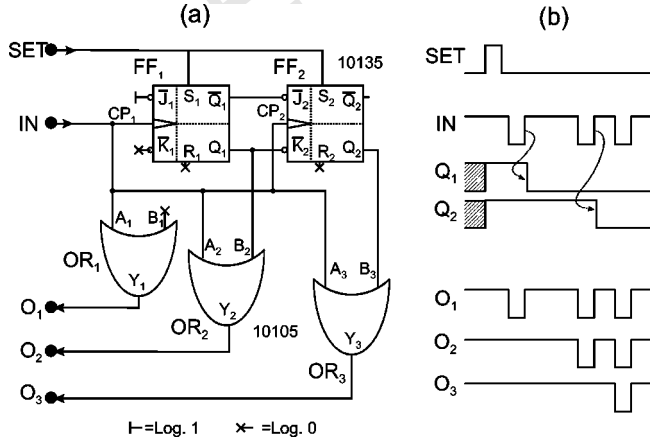

FIG. 4. Pulse router for multihit time- and position-sensitive detector. Timing diagram (a), circuit diagram (b). Consecutive input pulses (IN) are distributed to separate output lines (O_1, O_2, O_3). The circuit is designed in ECL technology to achieve a pulse pair resolution of 10 ns and a timing accuracy adequate for the 25 ps resolution of the TDC. Legend: FF: *JK*-flipflop, OR: OR gate.

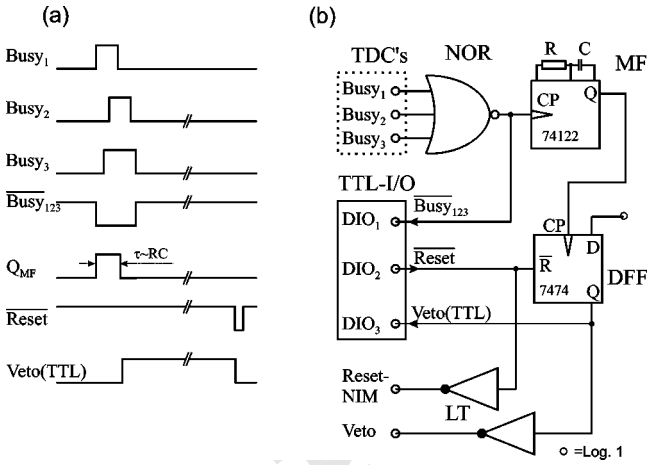

FIG. 5. Trigger logic and data readout sequence. Control of the data acquisition cycle: (a) timing diagram, (b) circuit diagram. Legend: NOR: NOR-gate, MF: monoflop, DFF: D-flipflop, LT: level translator TTL/NIM.

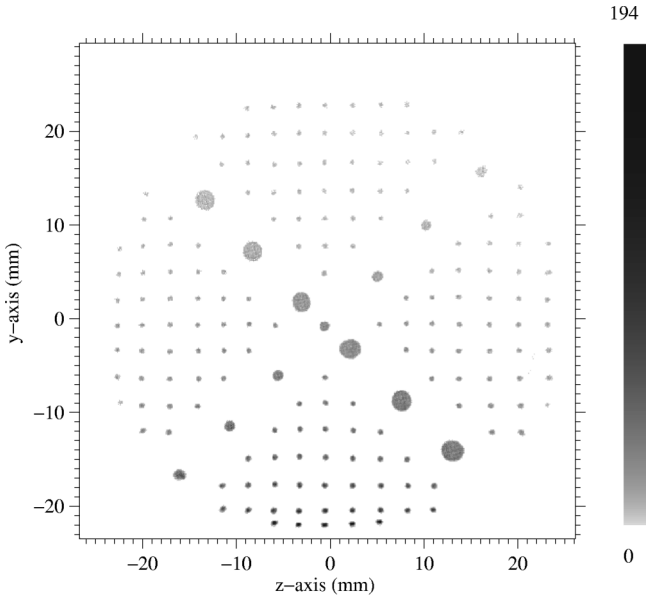

FIG. 6. Position calibration of the photofragment detector. A metal mask with a pattern of holes is placed in front of the detector. The detector is illuminated by fast neutral fragments. The distribution of the pulse arrival time differences at the waveguides terminals are shown in a two-dimensional histogram.

data readout cycle. However, it may take a considerable amount of time (several ms) between the end of a data readout and the occurrence of the next event. In this time, some of the router channels may already have toggled by false events. Therefore, we use pulse selectors (PS_1 and PS_2 in Fig. 3). We derive the set inputs for PR_1 and PR_3 from the first timing pulse of detector PSDA and the set input for PR_2 from the first timing pulse of detector PSDB. The pulse selector (PS) circuits to select the first and to suppress all following pulses are very similar to the routers Fig. 4. The input B_2 of gate OR_2 is connected to the $\overline{Q_1}$ output of FF_1 instead of Q_1. At the output O_2, the first input pulse (IN) appears, and all following input pulses are suppressed. Due to the cable delays between the CF discriminators and the router inputs shown in Fig. 3, the set pulses appear early enough at the pulse routers. The set pulses for the pulse selectors themselves (reset in Fig. 3) are generated at the end of the data readout by the trigger logic (TL).

2. Trigger logic and data readout sequence

The trigger logic (TL in Fig. 3) controls the basic measurement sequence and is connected to the Busy outputs of the TDCs, the Veto-inputs of the CF discriminators, the Reset inputs of the pulse selectors, and to the processor via a digital input/output interface (DIO) in the VME system. The trigger logic is built from TTL components. The circuit and the timing diagrams are shown in Fig. 5. The function of the trigger logic is closely intertwined with the software routine to control the digital interface (DIO) and to access the TDCs. The routine is written in C which allows a direct access to hardware registers without using assembler language. The Busy-outputs of the TDCs ($Busy_1$, $Busy_2$, $Busy_3$) are connected to the inputs of a NOR gate. A start pulse on any of the TDCs leads to a logic low transition at the output of the NOR gate ($\overline{Busy_{123}}$)which remains low until all of the TDCs have completed their conversions. The falling edge of $\overline{Busy_{123}}$ delayed by a monostable flipflop (MF) triggers a D flipflop (DFF). The D input of the flipflop is hard wired to logic high. The output of the flipflop (DFF) is converted to NIM level standard by level translators (LT) and produces the veto signals to inhibit the CF discriminators (Veto in Fig. 3). The time delay between the occurrence of the first busy signal and the assertion of the veto has to be adjusted depending on the fragmentation process investigated. The delay must be longer than the longest time difference which may occur between the first and the last fragment of the same event. Typical values are 300 ns–1.5 μs.

The processor is polling the Q output of the D flipflop via the digital interface (DIO_2) and is waiting for the logic-high status which indicates the occurrence of an event. Then, the processor has to poll $\overline{Busy_{123}}$(DIO_1) and to wait for the logic-high transition indicating that the TDCs have terminated conversion. Now, the readout of the binary TDC data is performed via the VME bus. The readout cycle is terminated by a computer-generated pulse (DIO_3) to reset the flipflop (DFF) and to clear the veto line. This pulse is level converted to provide the reset pulses for the pulse selectors (Reset NIM). Then, the system is ready and waiting for the next event.

D. Time and position calibration, consistency checks

The position of a fragment hit can in principle be determined using Eq. (2). To do this, we must accurately know the effective group velocity v_g, and have to take into account the lengths of all cable delays and the propagation delays of the electronic components in the signal paths. Therefore, we prefer an *in situ* calibration of the position scale. We place a stainless steel mask with a pattern of circular holes [Fig. 6(a)] in front of the detector. Then, the detector is ''illuminated'' by fast fragments produced by dissociative charge transfer of H_2^+, H_3^+, or N_2^+ in the cesium cell. The arrival time differences of the pulses at the terminals of the waveguides $t_{dy}=t_d-t_u$ and $t_{dz}=t_l-t_r$ are accumulated in two-dimensional histograms (Fig. 6). The regions

of high intensity in the histograms corresponding to the holes in the mask allow us to determine the constants (a_y, b_y, a_z, b_z) in the relation between the time differences and the positions according to the formula

$$y = a_y t_{dy} + b_y, \quad z = a_z t_{dz} + b_z. \tag{4}$$

To check and calibrate the measurement of the time differences between the events on the detector units PSDA and PSDB, pulses are produced by a time-and-delay generator (SRS, DG535) and injected into the timing amplifiers. This establishes the relation between the binary values of TDC_3 and the actual time differences of the pulses.

As discussed in Sec. II B, the sums t_{sy}, t_{sz} of the pulse arrival times at the waveguide terminals

$$t_{sy} = t_d + t_u, \quad t_{sz} = t_l + t_r, \tag{5}$$

are related to the time of the hit t_0 according to Eq. (3). For the fragment which starts the position measurement (TDC_1 or TDC_2), the values of t_{sy} and t_{sz} show narrow distributions (widths $\leqslant 3$ ns FWHM) centered at fixed values t_{0y} and t_{0z} which are given by the lengths of the waveguides and the inserted cable delays. The event is rejected if the values of the time sums (t_{sy}, t_{sz}) deviate too much from t_{0y} and t_{0z}, respectively. For a double-hit on one detector unit, the time sums (t_{sy}, t_{sz}) of the second fragment differ from those of the first one by twice the arrival time difference between the hits. The event is rejected in the case of a considerable disagreement between the information from the time sums and the arrival time differences measured by TDC_3. If two hits occur in a time interval smaller than v_g/L, the time sums can be used to assign the wire pulses to the events.

We have found that the multichannel plates produce afterpulses triggered by ion feedback. These afterpulses occur in a time range between 15 and 150 ns after the first pulse. The position of an afterpulse measured by the delay line anode is very close to that of the preceding pulse. Therefore, all double hits on the same detector unit which are spatially closer than 1 mm are rejected. In this way, afterpulses are eliminated at a minimal loss of detector collection efficiency.

III. DATA PROCESSING

From the measured positions and arrival time differences, we must determine the c.m. momentum vectors of the fragments. The data reduction strategies for a molecular breakup into an arbitrary number of fragments have been discussed in a separate publication from this laboratory.[31] In the following, the equations needed to study the dissociation of the H_3 molecule are given. The parent molecule with mass M and kinetic energy E_0 is moving with velocity vector $\mathbf{v}_0 = (v_{0x}, v_{0y}, v_{0z})$ in the laboratory frame. The transverse components (v_{0y}, v_{0z}) of the center-of-mass velocity are very small compared to the longitudinal component which means that to a good approximation $v_{0x} \approx \sqrt{2E_0/M}$. We neglect the finite size of the iteration region and assume that the fragmentation occurs at the origin of the laboratory coordinate system. The fragments are detected in a plane defined by $x = L$. The equations of motion of n fragments moving with velocity vectors $\mathbf{u}_i$ in the c.m. frame can be cast into the $3n$ relations:

$$(v_{0x} + u_{ix})(t_i - t_0) = L, \tag{6}$$

$$(v_{0y} + u_{iy})(t_i - t_0) = y_i, \tag{7}$$

$$(v_{0z} + u_{iz})(t_i - t_0) = z_i. \tag{8}$$

The time of fragmentation t_0 is not measured. We introduce the time differences between the ith and the first fragment $t_i - t_1 = L(u_{1x} - u_{ix})/[(v_{0x} + u_{ix})(v_{0x} + u_{1x})]$ and find the velocity differences d_{ix}:

$$d_{ix} \equiv u_{1x} - u_{ix} = (t_i - t_1)(v_{0x} + u_{ix})(v_{0x} + u_{1x})/L, \quad i = 2 \ldots n. \tag{9}$$

Using momentum conservation for the x component we determine the u_{ix} by

$$u_{1x} = \sum_{i=2}^{n} m_i d_{ix}/M, \quad u_{ix} = u_{1x} - d_{ix}, \quad i = 2 \ldots n. \tag{10}$$

Equations (9) and (10) constitute a fixed-point equation of the form $\mathbf{u}_x = T(\mathbf{u}_x)$ with an operator T mapping linear space $\mathcal{R}^n$ to itself. The solution is found by iteratively applying the operator T. Suitable start values are $u_{ix}^{(0)} = 0$. Improved values $u_{ix}^{(k+1)}$ are determined by resubstituting the vectors $u_{ix}^{(k)}$ into Eqs. (9) and (10) using the measured time differences $t_i - t_1$, the flight length L, and the longitudinal velocity v_{0x}. For the measured data in our spectrometer, three steps of iteration are sufficient to achieve a numerical accuracy far better than the experimental uncertainties.

After evaluating the longitudinal components u_{ix} of the fragment velocity vectors, we next determine the inverse flight times $\tilde{t}_i \equiv (t_i - t_0)^{-1} = (v_{0x} + u_{ix})/L$ from Eq. (6) and insert them into Eq. (7). Using momentum conservation, we find the transverse velocity components of the center-of-mass:

$$v_{0y} = \sum_i m_i y_i \tilde{t}_i / M, \tag{11}$$

and the fragment velocity components in the c.m. frame:

$$u_{iy} = y_i \tilde{t}_i - v_{0y}. \tag{12}$$

The equations for the z components from Eq. (8) instead of Eq. (7) are analogous. For three-body decay with equal fragment masses, we set $m_i = M/3$ which simplifies some of the formulas.

For two-body decay, we have to assign the fragment masses m_1 and m_2. Momentum conservation establishes the relations $u_{1x} = m_2 d_x/M$ and $u_{2x} = -m_1 d_x/M$ between the fragment velocity vectors and the relative velocity $\mathbf{d} \equiv \mathbf{u}_1 - \mathbf{u}_2$. We determine the mass ratio $Z = m_2/m_1$ from the measured quantities using the abbreviations $\Delta T = t_2 - t_1$ and $R_i = \sqrt{y_i^2 + z_i^2}$:

$$Z = -u_{1y}/u_{2y} \approx |R_1/R_2[1 - (v_{0x}\Delta T)/L]|. \tag{13}$$

The value of Z allows us to uniquely determine the masses m_1 and m_2. Eqs. (9) and (10) simplify to a single fix-point equation

$$d_x/v_{0x}=\frac{v_{0x}\Delta T}{L}\left(1+\frac{m_2-m_1}{M}d_x/v_{0x}-\frac{m_1m_2}{M^2}(d_x/v_{0x})^2\right), \tag{14}$$

which allows to iteratively calculate the longitudinal component of the fragment velocity difference d_x. According to Eqs. (11) and (12) the transverse components of the c.m. velocity v_{0y} and the velocity difference d_y are

$$v_{0y}=(m_1y_1+m_2y_2)\frac{v_{0x}}{ML}+(y_1-y_2)d_x\frac{m_1m_2}{M^2}, \tag{15}$$

$$d_y=(y_1-y_2)v_{0x}/L+(y_1m_2+y_2m_1)d_x/(ML). \tag{16}$$

Analogous equations hold for the z components.

IV. RESULTS

To test the multihit detector and the data acquisition and reduction procedures, we have studied the predissociation of the triatomic hydrogen molecule. We create a fast beam of H_3 in the metastable state $2p^2A_2''(N=K=0)$ by charge transfer of H_3^+ in cesium.[25] The intracavity dye laser is tuned to excite the metastable H_3 molecules in the vibrationless $3s^2A_1'(N=1, K=0)$ state at a frequency of 16 695 cm^{-1}. The excited state is known to decay within a few ns by several mechanisms:[25,36] predissociation into $H+H_2$ (v,J), radiative transitions followed by two-body decay, and three-body breakup into H+H+H.

A. Two-body decay of H_3

To investigate the two-body decay of H_3, coincidences between fragment pairs are collected. The coordinates (y_1,z_1) and (y_2,z_2) and the time difference t_2-t_1 of the fragment hits are measured. The subscripts 1 and 2 refer to the detector units PSDA and PSDB in Fig. 1, respectively. The spectrum of the mass ratio Z [c.f. Eq. (13)] is shown in Fig. 7(a). The two pronounced peaks at $Z=1/2$ and $Z=2$ are produced by two-body breakup of H_3 into $H+H_2$ fragment pairs. The continuous distribution with a maximum close to $Z=1$ is produced by three-body decay into H+H+H. Because of the momentum carried by the unobserved third hydrogen atom, momentum conservation does not hold for the two fragments measured in coincidence. This allows us, to distinguish between two- and three-body processes in the double hit events. The events fulfilling the condition

$$Z\in[0.45,0.55] \quad \text{or} \quad Z\in[1.82,2.22], \tag{17}$$

are evaluated as discussed in Sec. III. The mass ratio Z also allows us to decide whether the hydrogen atom was detected on PSDA $(Z<1, m_1=m_H)$ or PSDB $(Z>1, m_2=m_H)$. For each event, we determine the velocity difference vector **d** of the fragments by Eqs. (14)–(16), and the total kinetic energy release W:

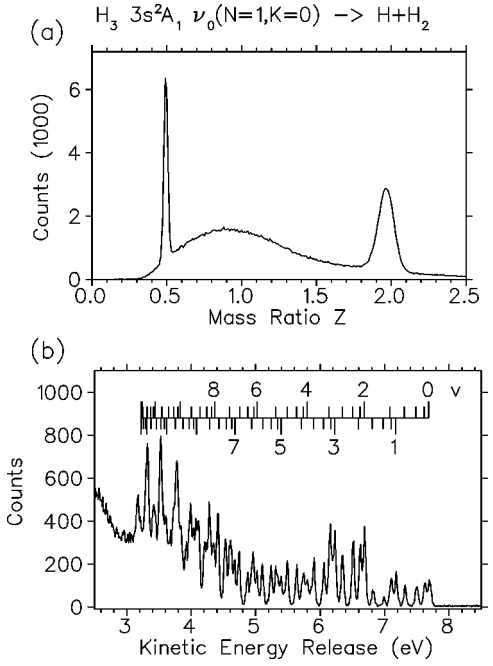

FIG. 7. Two-body decay of the vibrationless $3s^2A_1'(N=1, K=0)$ state of the H_3 molecule. (a) Spectrum of the mass ratio Z, (b) spectrum of the kinetic energy release W.

$$W=\frac{m_1m_2}{2M}(d_x^2+d_y^2+d_z^2), \tag{18}$$

in the c.m. frame. The spectrum of the kinetic energy release W produced by two-body decay of H_3 in the vibrationaless $3s^2A_1'(N=1, K=0)$ state is shown in Fig. 7(b). The pronounced discrete structures correspond to the rovibrational states of the $H_2(v,J)$ fragment as indicated by the stick spectrum. The energy resolution at $W=7$ eV is 35 meV (FWHM) which is appreciably better than that achieved in previous investigations.[26] For H_2 fragments with low vibrational quantum numbers, single rotational lines are resolved. This greatly facilitates the deconvolution of the measured spectrum. The good energy resolution opens the possibility to perform similar studies with deuterated species. The vectorial c.m. fragment velocities **d** determined for each event allow us to study the alignment of the fragment ejection angle with respect to the laser polarization. A comprehensive analysis of the two-body decay of H_3 and the determination of the branching ratios between the processes involved will be given in a separate publication.[32]

B. Three-body decay of H_3

1. Raw data

We have collected triple coincidences following three body decay of laser-prepared $H_3 3s^2A_1'(N=1, K=0)$ molecules and preprocessed the binary raw data as described in Sec. II D. To examine the performance of the data reduction, we have inspected the distributions of the hit positions and time differences of the correlated events. The hit positions are compatible with the sensitive regions of the detector which shows that the position calibration and the time sum checks Eq. (5) have been successful. For double hits on one

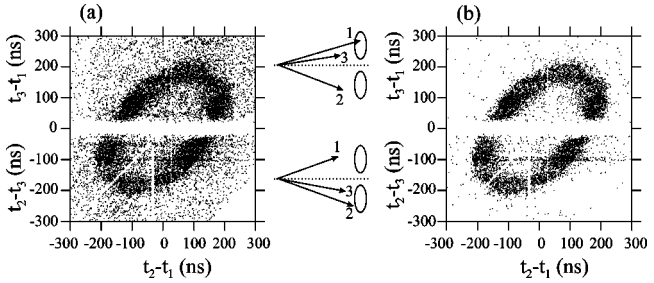

FIG. 8. Three body decay of vibrationless $H_3 3s^2A_1'(N=1, K=0)$: distributions of the arrival time differences of the three fragments. The subscripts of the arrival times t_i of each triple hit refer to: (1) first fragment detected by PSDA, (2) first fragment detected by PSDB. If the third fragment (3) hits PSDA, a point is drawn at t_3-t_1 vs t_2-t_1 falling into the upper part of the graph. If the third fragment hits PSDB, a point is plotted at t_2-t_3 vs t_2-t_1 in the lower part of the graph. (a) All events after data reduction are described in Sec. II D. (b) Only those events with a small transverse velocity of the c.m. compatible with the alignment and divergence of the parent molecular beam.

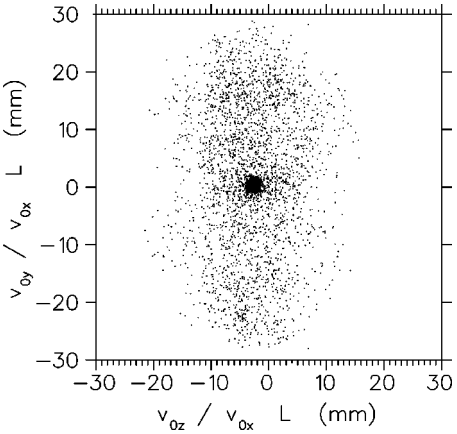

FIG. 9. Three-body decay of vibrationless $H_3 3s^2A_1'(N=1, K=0)$: distribution of the transverse velocity components of the center of mass. For each triple hit, the transverse velocity components v_{0y} and v_{0z} of the center of mass are calculated by Eq. (11). The points at $v_{0y}L/v_{0x}$ vs $v_{0z}L/v_{0x}$ reflect the locations where the center of mass hits the detector plane.

detector unit, we have plotted the time difference between the first and the second hit vs their spatial distance. We have found that afterpulses produced by the MCPs have been reliably recognized and successfully removed from the raw data set.

It is instructive to inspect the differences between the arrival times t_i of the three fragments. As schematically shown in Fig. 8, the subscripts of the arrival times refer to (1) the first fragment hit on PSDA, (2) the first fragment detected by PSDB, (3) the second hit on either PSDA or PSDB. If fragment (3) is detected by PSDA, t_3-t_1 vs t_2-t_1 is plotted and the points appear in the upper part of the diagram. If fragment (3) hits PSDB, we plot a point at t_2-t_3 vs t_2-t_1 which lies in the lower part of the diagram. We observe an elliptical, ring shaped region with high point density in Fig. 8(a). From a Monte Carlo simulation, we know that the coincident events produced by three-body decay of H_3 are located in this ring. The few false coincidences in Fig. 8(a) are homogeneously scattered in the plot. The horizontal empty region around the zero point of the ordinate in Fig. 8(a) reflects the finite double-hit resolution. The dead time of about 20 ns in this measurement is mainly caused by the output pulse widths of the CF discriminators which were widened to suppressed a ringing on the MCP timing pulses. However, Fig. 8(a) shows that the majority of the three-body events are accepted by the detector. The electronic circuits are suitable for a double pulse resolution as low as 10 ns which allows a further improvement of the overall collection efficiency. The small vertical region of low point density around $t_2-t_1=30$ ns and the vertial and diagonal empty stripes in the lower left quadrant of the plot are due to a cross talk between PSDA and PSDB.[33]

We then determine the three fragment momentum vectors $(\mathbf{u}_1,\mathbf{u}_2,\mathbf{u}_3)$ and the transverse velocity components (v_{0y},v_{0z}) of the center of mass using the data reduction algorithms Eqs. (9)–(12). In Fig. 9, the distribution of the transverse velocity components of the c.m. is shown. For each event, a point is drawn at $v_{0y}L/v_{0x}$ vs $v_{0z}L/v_{0x}$ corresponding to the position where the center of mass hits the detector plane. The events produced by three body decay are located in a circular region with a radius of 1.7 mm centered at ($z=-2.8$ mm, $y=0.9$ mm) which is compatible with the alignment and the divergence of the primary beam. The false coincidences are scattered almost homogeneously in this diagram. Consequently, the transverse velocity components of the center of mass can be used to suppress false coincidences. The effectivity of this criterion is visualized in the distribution of the time differences Fig. 8(b). Events with a transverse velocity of the center of mass incompatible with the alignment and divergence of the primary beam have been removed. Compared to Fig. 8(a), the number of scattered points in Fig. 8(b) is appreciably reduced while the density of true coincidences in the elliptical ring remains almost unaffected.

2. Projection of the six-fold differential cross section

By determining the three velocity vectors $\mathbf{u}_i$ in the c.m. frame, we measure the six-fold differential cross section for the photofragmentation of H_3. In this section, we present suitable projections to visualize this highly dimensional cross section. Due to momentum conservation $\Sigma_i m_i\mathbf{u}_i=0$, the three velocity vectors are linearly dependent and expand a plane. For each vector triple, three parameters are sufficient to describe the configuration of the three momenta in this plane. We may choose the absolute values of the momenta $p_i=m_i|\mathbf{u}_i|$ or the individual fragment energies $\epsilon_i=m_i\mathbf{u}_i^2/2$. It is, however, more convenient to use the total kinetic energy W:

$$W=\sum_1^3 m_i\mathbf{u}_i^2/2, \tag{19}$$

as one of the parameters. The kinetic energy release spectrum following three-body decay of the $H_3 3s^2A_1'(N=1, K=0)$ state is shown in Fig. 10 binned at 10 meV resolution. In this spectrum a narrow peak appears at 3.17 eV which is extremely close to the known energy of the initial state above the three-body limit, 3.155 eV.[25] The background in the spectrum is very small showing that the checks in the data reduction procedure are highly effective in eliminating

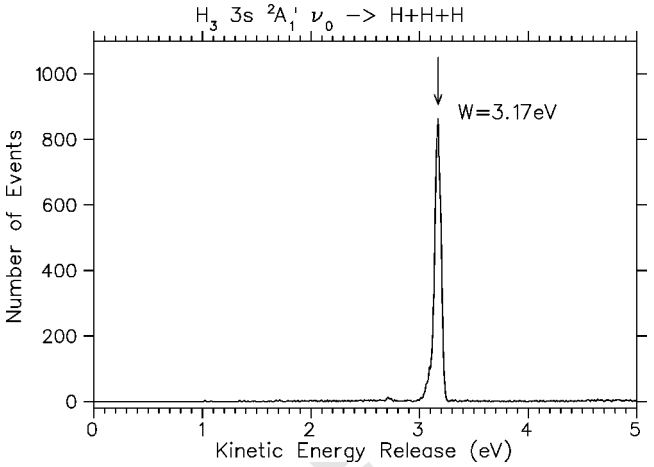

FIG. 10. Kinetic energy release in the three-body decay of vibrationless $H_3 3s^2A_1'(N=1, K=0)$.

false coincidences. The excellent agreement between the measured absolute value of W and the previously known state energy confirms the quality of the time- and position calibration of the detector.

An elegant way to present the remaining two parameters which describe the correlation among the fragment momenta was introduced by Dalitz.[34] For each event we plot $(\epsilon_3/W - 1/3)$ vs $[(\epsilon_2-\epsilon_1)/(W\sqrt{3})]$. The correspondence between the fragmentation configuration and the location in the plot is shown in Fig. 11(a). Energy and momentum conservation restrict the data points to the area inside a circle with radius 1/3 centered at the origin. In the case of three indistinguishable fragments, each configuration appears six times in the plot. As discussed by Perkins,[35] the Dalitz-plot conserves the phase space density. A dissociation process producing fragment momenta uniformly distributed in phase space would lead to a homogeneous point density in the Dalitz plot. In Fig. 11(b), the triple coincident events following three-body breakup of the laser-excited $H_3 3s^2A_1'(N=1, K=0)$ state are shown in a Dalitz plot. Only events within narrow kinetic energy regions around the strong peaks in Fig. 10 (3.05–3.25 eV) were selected. Since the three hydrogen atoms are indistinguishable, points are drawn in Fig. 11 for the six permutations of the fragment energies ϵ_i measured in each event. We have determined the geometric and electronic detector collection efficiency in a Monte Carlo simulation by generating a uniform distribution of fragmentation configurations and calculating the fragment propagation to the detector. Currently, detection of fragment triples where one of the momenta is close to zero (linear configuration) and therefore hits the space between the two detectors is excluded. Also, fragment hits which are close in time as well as in space ($H+H_2$ configuration) are suppressed due to the finite pulse pair resolution of 20 ns. The collection efficiency vanishes only for the linear and the $H+H_2$ configurations on the circle boundary. In the remainder of the Dalitz plot area, the detection efficiency shows a smooth variation. Therefore, the regions of high and low density in Fig. 11(b) are due to preferred fragmentation pathways in the molecular breakup process as discussed in Ref. 1.

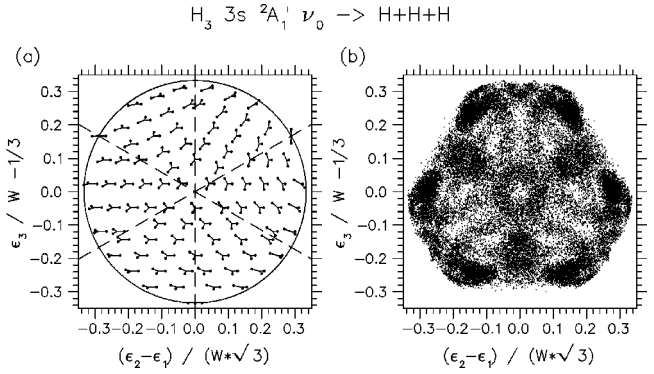

FIG. 11. Dalitz plot showing the final state distribution in molecular three body decay. (a) Correspondence between the location in the plot and the fragmentation configuration. (b) Final state distribution in three body decay of vibrationless $H_3 3s^2A_1'(N=1, K=0)$: into three hydrogen atoms H(1s) +H(1s)+H(1s).

The correction of the collection efficiencies and the determination of the branching between two- and three-body decay processes will be published separately.[32]

ACKNOWLEDGMENTS

This work is made possible by the generous support by Deutsche Forschungsgemeinschaft (SFB 276, TP C13). We are greatly indebted to Professor H. Helm (University of Freiburg) for his support and his continuous encouragement during the course of this work.

[1] U. Müller, Th. Eckert, M. Braun, and H. Helm, Phys. Rev. Lett. **83**, 2718 (1999).
[2] C. Maul, T. Haas, and K. H. Gericke, J. Phys. Chem. **101**, 6619 (1997); C. Maul and K. H. Gericke, Int. Rev. Phys. Chem. **16**, 1 (1997).
[3] Y. Tanaka, M. Kawaski, Y. Matsumi, H. Futsiwara, T. Ishiwata, L. J. Rogers, R. N. Doxin, and M. N. R. Ashfold, J. Chem. Phys. **109**, 1315 (1998).
[4] J. J. Lin, D. W. Hwang, Y. T. Lee, and X. Yang, J. Chem. Phys. **108**, 10061 (1998).
[5] M. Lange, O. Pfaff, U. Müller, and R. Brenn, Chem. Phys. **230**, 117 (1998).
[6] R. Moshammer, J. Ullrich, M. Unverzagt, W. Schmitt, P. Jardin, R. E. Olson, R. Doerner, V. Mergel, and H. Schmidt-Böcking, Nucl. Instrum. Methods Phys. Res. A **108**, 425 (1996).
[7] R. Doerner, V. Mergel, L. Spielberger, M. Achler, Kh. Khayyat, T. Vogt, H. Braeuning, O. Jagutzki, T. Weber, J. Ullrich, R. Moshammer, M. Unverzagt, W. Schmitt, H. Khemliche, M. H. Prior, C. L. Cocke, J. Feagin, R. E. Olson, and H. Schmidt-Böcking, Nucl. Instrum. Methods Phys. Res. B **124**, 225 (1997).
[8] Z. Vager, E. P. Kanter, G. Both, P. J. Cooney, A. Faibis, W. Koenig, B. J. Zabransky, and D. Zajfman, Phys. Rev. Lett. **57**, 2793 (1986).
[9] D. Kella, M. Algranati, H. Feldman, O. Heber, H. Kovner, E. Malkin, E. Miklazky, R. Naaman, D. Zajfman, and Z. Vager, Nucl. Instrum. Methods Phys. Res. A **329**, 440 (1990).
[10] E. P. Kanter, Z. Vager, G. Both, P. J. Cooney, A. Faibis, W. Koenig, B. J. Zabransky, and D. Zajfman, NIM B **24/25**, 321 (1987).
[11] D. Zajfman, E. P. Kanter, T. Graber, Z. Vager, and R. Naaman, Nucl. Instrum. Methods Phys. Res. B **67**, 22 (1992).
[12] O. Heber, D. Zajfman, D. Kella, Z. Vager, R. L. Watson, and V. Horvat, Nucl. Instrum. Methods Phys. Res. B **99**, 90 (1995).
[13] D. H. Chandler and P. L. Houston, J. Chem. Phys. **87**, 1445 (1987).
[14] B. L. G. Bakker, D. H. Parker, G. Hancocl, and G. A. D. Ritchie, Chem. Phys. Lett. **294**, 565 (1998).
[15] B. Buijsse, W. J. van der Zande, A. T. J. B. Eppink, D. H. Parker, B. R. Lewis, and S. T. Gibson, J. Chem. Phys. **108**, 7229 (1998).
[16] P. Samartzis, B. L. G. Bakker, T. P. Rakitzis, D. H. Parker, and T. N. Kitsopoulos, J. Chem. Phys. **110**, 5201 (1999).

[17] D. P. de Bruin and J. Los, Rev. Sci. Instrum. **53**, 1020 (1982).
[18] A. B. van der Kamp, L. D. A. Siebbeles, and W. J. van der Zande, J. Chem. Phys. **101**, 9271 (1994).
[19] L. D. Gardner, M. M. Graff, and J. L. Kohl, Rev. Sci. Instrum. **57**, 177 (1986).
[20] R. E. Continetti, D. R. Cyr, D. L. Osborn, D. J. Leahy, and D. M. Neumark, J. Chem. Phys. **99**, 2616 (1993).
[21] K. A. Hanold, A. K. Luong, and R. E. Continetti, J. Chem. Phys. **109**, 9215 (1998).
[22] K. A. Hanold, A. K. Luong, T. G. Clements, and R. E. Continetti, Rev. Sci. Instrum. **70**, 2268 (1999).
[23] H. Helm and P. C. Cosby, J. Chem. Phys. **90**, 4208 (1989).
[24] C. W. Walter, P. C. Cosby, and H. Helm, J. Chem. Phys. **99**, 3553 (1993).
[25] P. C. Cosby and H. Helm, Phys. Rev. Lett. **61**, 298 (1988).
[26] U. Müller and P. C. Cosby, J. Chem. Phys. **105**, 3532 (1996).
[27] K. Beckord, J. Becker, U. Werner, and H. O. Lutz, J. Phys. B **27**, L585 (1994).
[28] Z. Amitay and D. Zajfman, Rev. Sci. Instrum. **68**, 1387 (1997).
[29] S. E. Sobottka and M. B. Williams, IEEE Trans. Nucl. Sci. **35**, 348 (1988).
[30] O. Jagutzki, V. Mergel, K. Ullmann-Pfleger, L. Spielberger, U. Meyer, and H. Schmidt-Böcking, Proc. SPIE 19.7.-24.7.(1998).
[31] M. Beckert and U. Müller, Z. Phys. D (submitted).
[32] M. Beckert and U. Müller, to be published.
[33] R. N. Zare. Ber. Bunsenges. Phys. Chem. **86**, 422 (1982).
[34] R. H. Dalitz, Philos. Mag. **44**, 1068 (1953); Annu. Rev. Nucl. Sci. **13**, 339 (1963).
[35] D. H. Perkins, *Introduction to High Energy Physics* (Addison-Wesley, Reading, MA, 1987), p. 119.
[36] U. Müller and P. C. Cosby, Phys. Rev. A (1999).